Strength ranking for interfaces between a TiN hard coating and microstructural constituents of high speed steel determined by micromechanical testing

Matthias Gsellmann [a], Thomas Klünsner [a,*], Christian Mitterer [b], Martin Krobath [a], Michael Wurmshuber [b], Harald Leitner [c], Werner Ecker [a], Stefan Marsoner [a], Verena Maier-Kiener [b], Daniel Kiener [b], Gerald Ressel [a]

[a] Materials Center Leoben Forschung GmbH (MCL), Roseggerstraße 12, 8700 Leoben, Austria
[b] Department of Materials Science, Montanuniversität Leoben, Franz-Josef-Straße 18, 8700 Leoben, Austria
[c] Voestalpine Böhler Edelstahl GmbH & Co KG – Mariazellerstraße 25, 8605 Kapfenberg, Austria

ARTICLE INFO

ABSTRACT

Knowledge about the adhesion of protective hard coatings on tool materials is of great importance to understand their failure mechanisms in metalworking. Until now, common techniques such as scratch and indentation tests are used to establish a qualitative ranking of a coating's adhesion on various substrate materials. Nevertheless, there is a lack of quantitative measures to describe the strength of the interfaces between individual microstructural constituents of substrate-coating composites. The current work investigates the interfacial strength and thus the adhesion of TiN deposited as a hard coating on an MC-type carbide, an M_6C-type carbide and on martensite being constituents of high speed steels. Tensile stresses were introduced at the interface between TiN and the individual microstructural constituents of a high speed steel via micromechanical testing of a novel MSC specimen within a scanning electron microscope. The tested MSC specimens were subsequently investigated in detail by scanning electron microscopy. Evaluation of the interface stress at fracture via finite element analysis yielded a ranking in interface strength and therefore coating adhesion in a sequence from high to low strength values from MC/TiN over M_6C/TiN to martensite/TiN.

© 2021 The Author(s). Published by Elsevier Ltd. This is an open access article under the CC BY-NC-ND license (http://creativecommons.org/licenses/by-nc-nd/4.0/).

1. Introduction

Hard coatings are of great importance to increase the performance and lifetime of metalworking tools [1-3]. To ensure integrity of the used substrate-coating systems during operation, excellent coating adhesion is essential. In many cases, substrate materials for cutting tools are made of high speed steels (HSS) containing various types of metal carbides, which are usually of type MC and M_6C, embedded in a martensitic matrix. During cutting application, the hard coating may be removed, exposing the substrate material to increasingly harsh conditions while cutting, since it loses the coating's function as a protection against abrasive and adhesive wear [4] as well as a thermal barrier [5,6]. Therefore, excellent coating adhesion is necessary to avoid premature coating decohesion [3,7]. Until now, many test methods are known to assess the quality of the coating and to classify its adhesion properties. Technological test methods, such as scratch or Rockwell indentation (HRC) test, are commonly used to empirically compare the quality of the coating adhesion [8-13]. In general, adhesion or, more precisely, adhesion strength means bonding strength between the substrate material and the coating [10]. Coating adhesion is influenced to a large extent by the substrate properties including its surface topography and its mechanical properties, such as yield strength [14,15]. Also, interfacial failure may be affected by the presence of defects, chemical contamination or the stress state of the coating [14,16].

This situation is even more complex for the commonly used tool materials consisting of multiple phases, where different interfaces are present between these phases and the hard coating. Therefore, information about the properties of the interfaces between these individual microstructural constituents and the coating is of immense importance to understand the properties and thus performance of the entire substrate-coating composite.

Common adhesion test methods usually investigate a region of hundreds of square microns, which contain a large amount of different microstructural constituents, e.g. metal carbides in HSS [17]. Consequently, the obtained adhesion quality represents an

---

averaged quantity influenced by the contributions of all microstructural constituents within the tested region. Thus, knowledge about the local adhesion of those individual constituents is essential to understand the influence of each on the failure behaviour of coated HSS, building a fundamental base for future material design. Up to now, only a few studies have been conducted to estimate the effect of carbide content on the coating adhesion on HSS substrates. A beneficial effect of MC carbide density at the interface of a titanium nitride (TiN) coated HS 6–5-2 tool steel has been documented by means of scratch testing in the 1980s [18]. It was concluded that coating adhesion increases with rising MC carbide density, as an increase of the critical force obtained during scratch testing has been observed, which is interpreted as a measure for coating adhesion. Please note that the expression "carbide density" refers to the number of carbides per unit area of the TiN steel interface. This was explained by an epitaxial growth of the TiN coating on the MC carbide due to the small difference between their lattice parameters and therefore a strong bonding strength [19].

Previous studies have investigated the properties of interfaces by determination of their toughness and strength on various substrate-coating systems using different micromechanical test methods. The interface toughness has been determined via interface nanoindentation by using the obtained critical force for interface cracks, the interfacial crack length and the mechanical properties of substrate and coating [20] or via microbending beams composed of steel and a diamond-like carbon coating or silicon and SiOx, respectively, by calculating the fracture toughness K_{IC} of the interface [21,22]. The interfacial strength between amorphous-crystalline nanolayers was estimated by means of microcompression testing using the obtained stress–strain behaviour and electron microscopy observation of the tested micropillar [23,24]. The aim of all these test methods is to separate the coating from the substrate by exceeding its bonding strength, which may be equated with interface strength. In some studies, investigations on micropillars with inclined interfaces to achieve shear stresses at the interface have been conducted [23,25], as the critical stresses for substrate-coating composites were described as shear stress [26,27] or a combination of shear and tensile stresses [28]. In most cutting applications where coated cutting tools are used, shear and compressive stresses act on the interface between substrate and coating. However, effects such as local plasticity or surface roughness may cause local tensile stress components there. Note, that today there is no established technique that would facilitate study of the local interface strength between individual microstructural constituents of HSS and a hard coating. Hence, within the current study, the local interface strength of MC, M_6C carbides and the martensitic matrix coated with TiN has been investigated using a novel micromechanical test setup. A load spectrum composesing of normal, shear and tensile loads was applied to the substrate-coating interface, simulating loads acting in real-world metalworking tools, for example when a chip flows over the surface of a milling or drilling tool's rake face [3,29]. For this investigation, a novel micropillar geometry has been used and tested in-situ in a scanning electron microscope (SEM). By means of finite element (FE) simulation, the stresses acting at the substrate-coating interface region at the moment of failure were described and quantitatively associated with interface strength. Detailed investigations of the fractured specimens using SEM were performed to clarify the origin of fracture. Furthermore, influencing factors such as coating stress, interfacial flaw distribution as well as the well-known size effect that need to be considered when interpreting strength values will be discussed.

2. Methodological approach

2.1. Experimental details

2.1.1. Preparation of coated HSS specimens

Within this study, the aluminium alloyed high speed steel HS 4–4-2–5 produced by voestalpine BÖHLER Edelstahl was investigated. It consists of tungsten-, molybdenum- and iron-rich M_6C and vanadium-rich MC carbides, embedded in a tempered martensitic matrix, see Fig. 1.

The chemical composition of the investigated material is listed in Table 1 and was determined using a wet-chemical process.

One cylindrical specimen of 10 mm in height and 20 mm in diameter was cut from a hot-rolled and soft-annealed steel bar of the same diameter. This specimen was subsequently heat-treated with an austenitization step at 1190 °C for 0.5 h and a triple tempering process at 560 °C for 1.5 h. After heat treatment, the specimen contained 1.2 vol% MC and 2.0 vol% M_6C, determined by means of a quantitative image analysis of a statistically representative cross sectional area via SEM. Subsequently, the specimen surface was chemically polished using an oxidative polishing suspension to enhance carbide visibility in light optical microscopes, as carbides etch slower than the martensitic matrix. An area with a large quantity of carbides was marked by Vickers imprints. The marked position was imaged using the backscattered electron (BSE) contrast mode of a Zeiss EVO MA25 SEM.

About 2 μm thick TiN coatings were deposited by cathodic arc evaporation. The process included a two-step plasma pretreatment with a glow discharge and a metal ion etching process performed by voestalpine eifeler Vacotec GmbH [30]. The HSS substrate was heated to a temperature of 400 ° – 450 °C prior to coating deposition. The subsequent plasma-etching in argon was conducted to remove contaminations from the substrate surface. Furthermore, to improve coating adhesion, the specimen was Ti^+ ion etched at a bias voltage V_b of −500 V to −1000 V. The coating was finally synthesized using six grade 2 Ti cathodes, which were arranged in columns, whereby three cathodes were evenly distributed over the chamber height for each column. For deposition, a cathode current of 60 A, a negative DC substrate bias voltage V_b of −150 V and a nitrogen partial pressure of 1.2 Pa was used at a substrate temperature of 400 °C. The samples were mounted in threefold rotation with a minimum cathode to substrate distance of 150 mm. Despite the deposited TiN coating, a carbide relief at the specimen surface resulting from the mentioned chemical
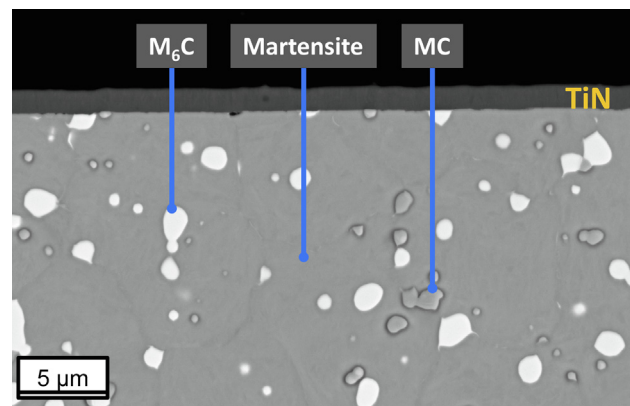

Fig. 1. Characteristic microstructure of the investigated HSS material showing M_6C carbides in white, MC carbides in light grey and the martensitic matrix in dark grey.

Table 1
Nominal chemical composition of the investigated steel grade HS 4–4–2–5 in wt.%.

	C	Cr	Mo	V	W	Co	Al	Fe
Content [wt.%]	0.93	3.87	3.93	1.90	4.00	4.59	0.57	Balance

polishing process was finally visible. The corresponding carbide type was assigned by BSE contrast in the SEM [17].

2.1.2. MSC specimen preparation and stress estimation

The area marked by Vickers imprints was extracted from the TiN coated cylindrical specimen by cutting, grinding and polishing to achieve a rectangular geometry of 10 mm length, 2.5 mm height and 300 μm width. Subsequent thinning of the specimen using a Hitachi IM4000 + IonSlicer ensured the optimum width of 40 μm for focused ion beam (FIB) based specimen preparation [31]. The final micropillar geometry named "micro shear compression" (MSC) specimen, shown schematically in Fig. 2, was prepared by means of FIB milling using a Zeiss Auriga 40 SEM.

Fig. 2 presents a schematic visualization of the used MSC specimen geometry, in which the MSC specimen base is composed of either M_6C, MC or the martensitic matrix, referred to as matrix in the current work. An inclined surface was used to apply the load F, to achieve combined shear and compression load components at the substrate-coating interface, as they also act at the rake face of cutting tools [29,32]. Since shear load is interpreted to contribute to coating failure [26,33], the side of the MSC specimen used for loading was inclined by an angle α of about 60° to induce a significant shear load component at the interface. This angle leads to a shear to compression ratio $\frac{\tau}{\sigma}$ of about 1.7. Details of the MSC specimen geometry for both investigated carbide types and the matrix are listed in Table 2. The three MSC specimens exhibit different dimensions due to the different sizes of the individual phases M_6C, MC and the matrix, which are inherent to HSS. This means that for certain interfaces the testable interface areas are given by the microstructural constituents' typical dimensions and that thus sample size is intrinsically limited.

The following equations were used to describe the interfacial stresses present at the interface at fracture of the MSC specimen in a first approximation [34]:

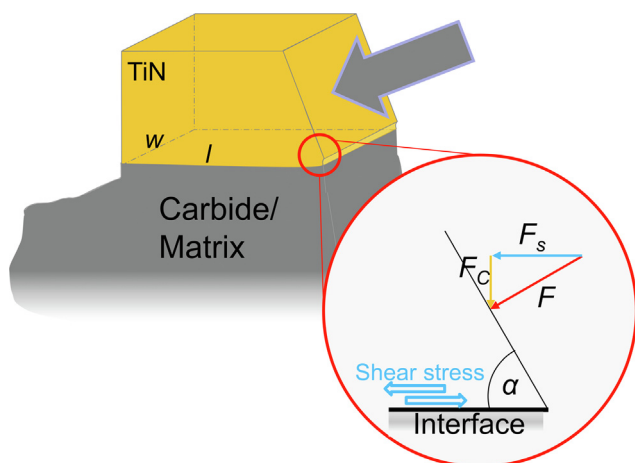$$\tau = \frac{F_S}{A_P} \cdot sin\alpha; \sigma_C = \frac{F_C}{A_P} \cdot cos\alpha \qquad (1)$$

Fig. 2. Scheme of the FIB-milled micro shear compression (MSC) specimen showing the load F acting at the interface while testing with its shear (F_S) and compression (F_C) components with respect to the interface orientation. The surface loaded via a flat punch indenter in direction of the gray arrow is inclined with regard to the TiN/substrate interface by an angle α of approximately 60°.

where F_S represents the shear force, F_C the compression force, τ the shear stress, σ_c the compression stress and α the inclination angle indicated in Fig. 2. Eq. (1) correlates with the geometrical arrangement of the MSC specimen used in the present study (see Fig. 2).

2.1.3. Micromechanical testing

In order to induce local tensile stresses at the substrate-coating interface combined with shear and compression load, micromechanical tests were conducted. Thereby, the MSC specimens were loaded using a UNAT-SEM indenter provided by Zwick mounted within a Zeiss LEO 982 field emission gun SEM (FEG-SEM). The indenter tip was a 19 μm diameter flat punch provided by Synton-MDP. The load was applied under displacement control with a maximum range of 0.5 μm per load step for the M_6C/TiN, 1.5 μm for the MC/TiN and 0.8 μm for the matrix/TiN MSC specimen. The maximum displacement rate was set to 10 nm/s. A load–displacement curve was recorded for each MSC specimen. Before and after testing, detailed characterization of the pillars was conducted using a Zeiss Auriga 40 FEG-SEM equipped with energy dispersive spectroscopy (EDS).

2.1.4. Nanoindentation testing

Nanoindentation experiments were conducted to gain information on the deformation behaviour of the martensitic matrix on a platform nanoindenter G200 (KLA, formerly Keysight, Agilent) equipped with a continuous stiffness measurement unit in order to measure contact stiffness, and thus hardness, flow stress as well as Young's modulus, continuously over indentation depth by superimposing an alternating displacement signal (2 nm, 45 Hz). Firstly, standard hardness and Young's modulus were measured with a diamond Berkovich tip (Synton-MDP) in indentation strain-rate controlled mode to 2000 nm indentation depth and all analysis were accomplished as suggested by Oliver & Pharr [35] for continuous measurement testing of contact stiffness by a dynamic technique. Additionally, local mechanical flow curves of the matrix material were determined according to the procedures recently described by Leitner et al. [36]. Therefore, three different conical diamond indentation tips with nominal radii of 5, 10 or 20 μm (Synton-MDP) were utilized. Before testing, the actual tip shape area functions of the conical indentation tips were calculated from reference indentations in fused quartz in order to consider deviations from perfect spherical geometries. Following, six indentations each were run in constant strain-rate mode ($0.005 \, s^{-1}$) to 22% representative strain (cone5) or to the maximum load capacity of the indentation system (650 mN) corresponding to 9.5% (Cone20) and 15.5% (Cone10) representative strain. Finally, indentation depth and thus strain dependent constraint factors were experimentally assessed for each spherical indentation test and applied to the hardness data to receive a local mechanical flow curve [36]. The resulting stress strain relationship is shown in Fig. 3.

2.2. Finite element simulation

FE simulations were conducted to estimate the stress states at the interfaces at the respective experimentally determined fracture load, in particular the maximum principal stresses. The simulations were conducted using the commercial finite element software package Abaqus [37]. The simulation models display the

Table 2

Geometric dimensions of the MSC specimens containing the interfaces M_6C/TiN, MC/TiN and matrix/TiN, where l represents the length, w the width (Fig. 2), t_{TiN} the coating thickness, A_{Pillar} the interface area of the MSC specimen, and α the inclination angle (the slight differences in coating thicknesses stem from re-deposition, subsequently removed during FIB milling).

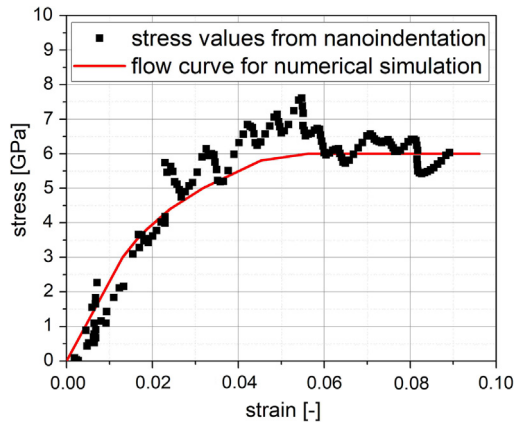|	l [µm]	w [µm]	t_{TiN} [µm]	A_{Pillar} [µm^2]	α [°]
M_6C/TiN	1.90	2.00	1.30	4.00	57.00
MC/TiN	3.90	4.90	1.50	18.90	59.50
Matrix/TiN	2.94	2.30	1.66	6.76	60.00

Fig. 3. Stress strain relationship from nanoindentation experiments represented by squares and a fit curve defining the plastic material behaviour of the matrix material in numerical simulations.

idealized geometries of the pillars without any surface or interface roughness, see Fig. 4.

Roughly 20,000 hexahedron elements with linear shape functions were used to discretize the pillars, the element size in the relevant regions was approximately 0.1 µm. Elasto-plastic material behaviour was assumed for the martensitic matrix, Young's modulus and the plastic flow curve were derived from the nanoindentation experiments, see Fig. 3. All other material phases were modelled with linear elastic material behaviour. The implemented material characteristics are summarized in Table 3.

To account for the influence of residual stresses, the bi-axial in-plane compressive residual stress values in the coating were varied to be 0, −2 and −5 GPa, respectively, for all investigated systems. An analytically rigid surface represents the indenter, where the interaction between indenter and pillar is defined as surface-to-surface contact with finite sliding conditions and an isotropic Coulomb friction coefficient of 0.2. The kinematics of the indenter was prescribed and corresponds to the displacement-controlled movement of the indenter in the experiment. The boundary conditions of the MSC specimens were defined to resemble the real test setup and also consider the lateral clamping of the rectangular sample in the sample holder, see Fig. 4a).

The reaction force of the indenter's reference point in the direction of the prescribed movement is correlated to measured forces of the experiments to estimate the point of maximum loading in the simulation.

3. Results

3.1. Micromechanical testing of MSC specimens

The load–displacement curve obtained under monotonously increased load of the M_6C/TiN, the MC/TiN and the matrix/TiN MSC specimens is shown in Fig. 5. The almost linear increase of the force suggests the absence of misalignment [40] and a predominantly elastic material behaviour of the carbide-coating systems
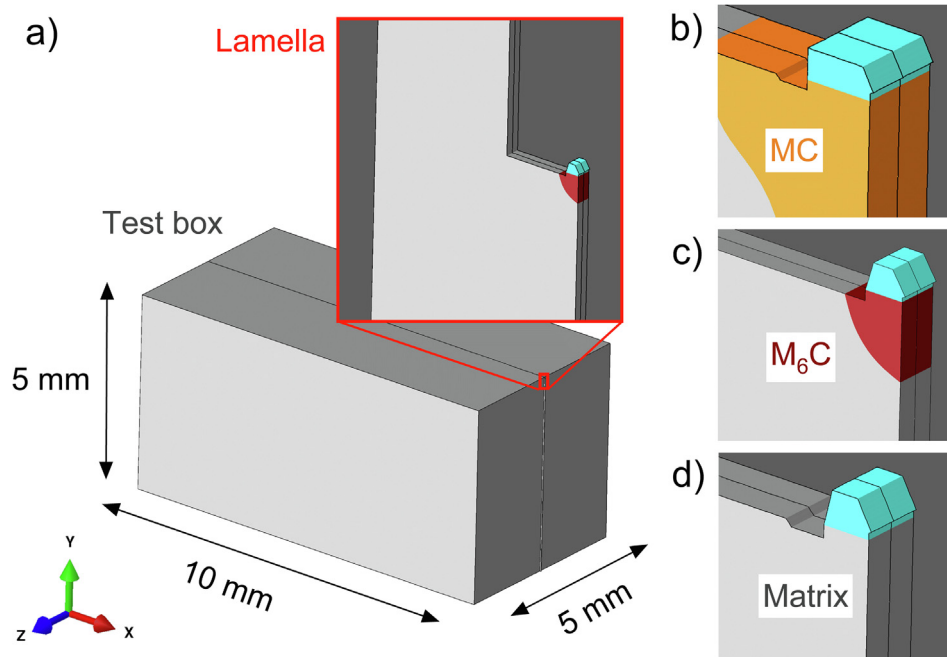

Fig. 4. a) Geometric definitions of the macroscopic test box used for FE simulation with enlarged lamella region. (b)–(d) the three investigated pillar geometries with constant magnification factor, the geometric specifications are listed in Table 2.

Table 3

Material specifications of the TiN coating [38], the carbides [39] and the martensitic matrix used for the FE model.

	TiN	MC	M_6C	Matrix
Material behaviour	Elastic	Elastic	Elastic	Elasto-plastic
Young's modulus [GPa]	520	338	318	230
Poisson's ratio [-]	0.21	0.25	0.25	0.30
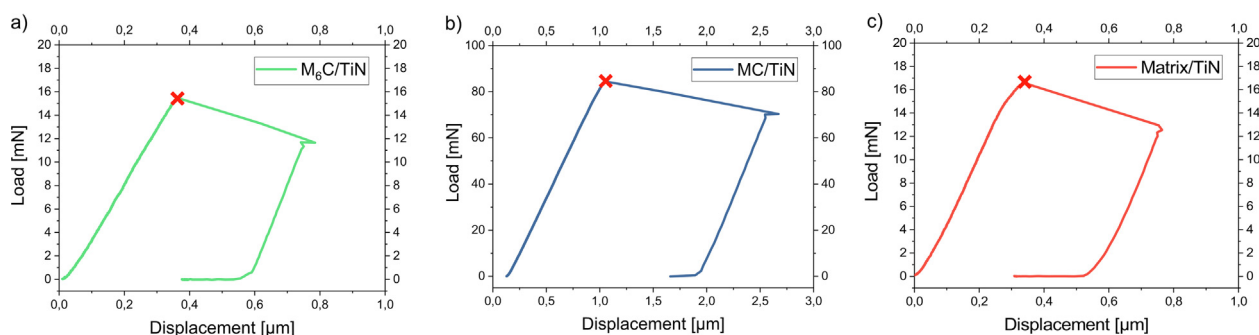
Fig. 5. Load-displacement curves of a) the M_6C/TiN, b) the MC/TiN and c) the matrix/TiN MSC specimen. Fracture occurred at maximum force marked by red crosses. (For interpretation of the references to colour in this figure legend, the reader is referred to the web version of this article.)

until fracture, as all components have high Young's moduli [39,41]. The slight kink in the load–displacement curve of the matrix/TiN MSC specimen before reaching the maximum force indicates that plastification occurred in the pillar prior to its failure, see Fig. 5c). The drop of the force after reaching its maximum, marked with a red cross in Fig. 5, correlates with the moment of failure of the MSC specimens. The increase of the displacement associated with the force drop before the obligatory unloading step stems from the release of elastic energy stored in the loaded specimen-indenter system, which obviously occurs in a way that it cannot be compensated by the feedback control of the indentation device and will be referred to as spring back.

The shear stress as well as the compression stress acting on the interfaces between M_6C/TiN, MC/TiN and matrix/TiN at the moment of fracture were estimated using Eq. (1) from section 2.1.2, inserting the forces F_{max} observed at the moment of fracture, as listed in Table 4.

In addition to the load–displacement curves, SEM images were taken in-situ during loading to investigate deformation and fracture of the MSC specimens during the test. The sequence of SEM micrographs in Fig. 6 shows (i) the initial state before contact between indenter and MSC specimen, (ii) the image collected when fracture occurred and (iii) the final state after fracture of the MSC specimen for the M_6C/TiN interface (Fig. 6a)-c)), the MC/TiN interface (Fig. 6d)-f)) and the matrix/TiN interface (Fig. 6g)-i)), respectively. Please note, that specimen fracture occurred at a point in time when the image acquisition process was incomplete in Fig. 6b), Fig. 6e) and Fig. 6h). The named images show the state of the image acquisition with scanning starting from the top of the image and the new image overlaying the previously acquired one. Therefore, the images illustrate the state of the specimens just after the moment of fracture in the image part above the horizontal "transition line" indicated by horizontal orange arrows, and just before the moment of fracture below these lines. For an animated visualization of the whole testing procedure of each MSC specimen, videos have been provided, see supplementary material.

Due to the different electron interaction of the constituents, a clear distinction of the light grey M_6C carbide, the dark grey TiN coating and the interface between them is apparent in Fig. 6a)-c). Fracture occurred directly at the interface, as Fig. 6b) clearly indicates, which infers that failure starts from the interface between

carbide and TiN coating. The fragments of the MSC specimen visible in Fig. 6c) are interpreted to have formed due to the instantaneous release of stored elastic energy upon fracture and the associated push of the indenter in the loading direction, compare Fig. 5b). The sequence of SEM micrographs for the MC/TiN MSC specimen, see Fig. 6d)-f) shows a completely fractured MSC specimen after the completed test, see Fig. 6f), which makes it almost impossible to identify the fracture origin. However, a similar behaviour as depicted in Fig. 6a)-c) can directly be observed for the matrix/TiN MSC specimen again, displayed in Fig. 6g)-i), where the coating is displaced along a direction parallel to the interface.

In order to obtain an overview of the remains of the MSC specimens after testing, detailed investigations were carried out using a FEG-SEM, see Fig. 7. The green arrows in Fig. 7a) mark some fragments of the TiN coating, identified by their Ti content observed via EDS, for the M_6C/TiN MSC specimen.

The MSC specimen's top surface that remains after testing exhibits small grooves marked by orange arrows in Fig. 7b). These grooves stem from HSS sample surface preparation via grinding prior to coating deposition. EDS analysis did not show any Ti on the fracture surface indicating a sharp separation of coating and carbide and a fracture path located at or very close to the carbide-coating interface.

The larger dimensions of the MC/TiN MSC specimen compared to its M_6C/TiN counterpart and the larger amount of elastic energy released upon fracture leads to a completely destroyed MSC specimen in the case of the MC/TiN pillar, see Fig. 7c) and d). Most of the fragments marked by green arrows in Fig. 7c) were assigned to the MC carbide by EDS measurements. Despite detailed investigation of the tested MC/TiN MSC specimen, no certain information about the nature or location of the fracture origin can be given for this pillar.

The coating of the matrix/TiN MSC specimen, however, remained on the MSC specimen base after testing and was not destroyed, see Fig. 7e). The coating part was slightly rotated, see red arrows in Fig. 7e), and shifted in loading direction, as clearly visible in Fig. 7f), indicating a failure at the interface, as also shown in Fig. 7g). Furthermore, the top face of the MSC specimen's coating that was originally parallel to the top face of the surrounding martensite surface seen in Fig. 7g), appears to be tilted counter-clockwise relative to this area after testing.

Table 4

Fracture stress values estimated using Eq. (1) for the interfaces between M_6C/TiN, MC/TiN and matrix/TiN in the investigated MSC specimens. F_{max} represents the maximum force applied to the MSC specimen, τ the estimated shear stress, σ_C the estimated compression stress and τ/σ the ratio of shear and compression.

	F_{max} [mN]	τ [MPa]	σ_C [MPa]	τ/σ [-]
M_6C/TiN	15.50	3290	2136	1.54
MC/TiN	84.50	3850	2268	1.70
Matrix/TiN	16.60	2126	1228	1.73
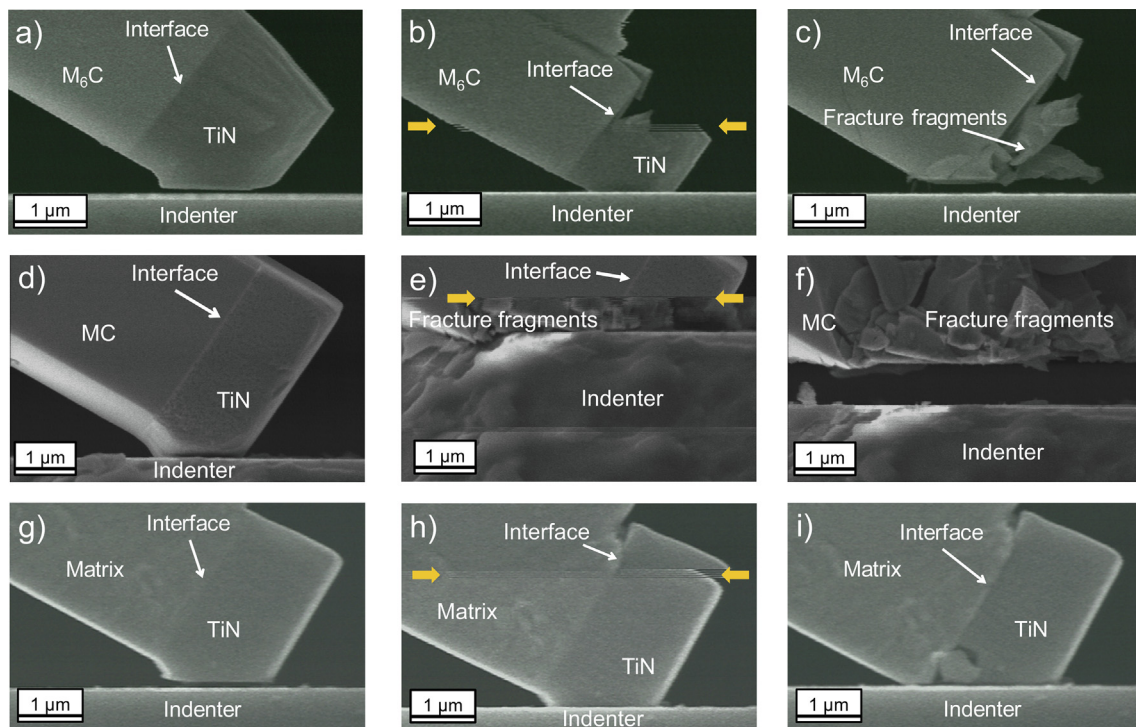
Fig. 6. Sequences of SEM micrographs showing the initial state, a state immediately after fracture and the final state after testing for the M_6C/TiN (a)–c)), the MC/TiN (d)–f)) and the matrix/TiN MSC specimen (g)–i)). Fig. 6(e) and Fig. 6f) show mainly fracture fragments, as the pillar was destroyed by the collision of specimen and indenter after the fracture event.

3.2. Stress distribution at the interfaces

The distribution of maximum principal stresses at the interfaces, that are the most positive, i.e. most tensile ones of the principal stress components, was evaluated at maximum load for all investigated MSC specimens and the systems with bi-axial compressive residual stresses of – 2 GPa are compared in Fig. 8, as this value is common in coatings for metalworking tools [42]. The contour plots demonstrate that even though the pillars are dominated by compressive stresses, they still exhibit tensile components within the interfaces relevant to crack opening and therefore failure in metals [43] and especially ceramic materials [44]. The direction of the maximum, in the sense of most tensile, principal stress is all roughly perpendicular to the loading direction, as illustrated by the arrows in Fig. 8b), Fig. 8d) and Fig. 8f). Within the investigated range, these directions are hardly dependent on the coating residual stresses. In all specimens the most positive maximum principal stresses are located at the sides of the pillars and decrease towards the centres of their cross sections.

The maximum principal stress of the MC/TiN MSC specimen is significantly higher than that of the M_6C/TiN MSC specimen. Moreover, both MSC specimens containing carbides depict much higher maximum principal stresses than the MSC specimen containing

the martensitic matrix, shown in Fig. 9. With rising compressive residual stresses within the coating and a constant external loading, the maximum principal stress calculated of the interfaces increases due to increasing triaxiality of the stress state.

4. Discussion

The following points have to be considered when interpreting the results. The observed differences in the external loads at fracture between all MSC specimens can be explained by the different specimen dimensions on the one hand, see Table 2, and differences in their interface strength on the other hand. Most frequently, the term strength refers to material failure under uniaxial tensile load under standardized conditions; however, also shear strength or bending strength can be used to describe the failure behaviour of a material [45]. For the more complex case of composite materials, the interface strength between the constituent materials that differ in their mechanical properties, may significantly determine the composite's failure behaviour [26]. Since there is no commonly accepted definition of interface strength, we here denote the maximum principal stress value calculated in the FE simulations present at the interface as interface strength under combined shear
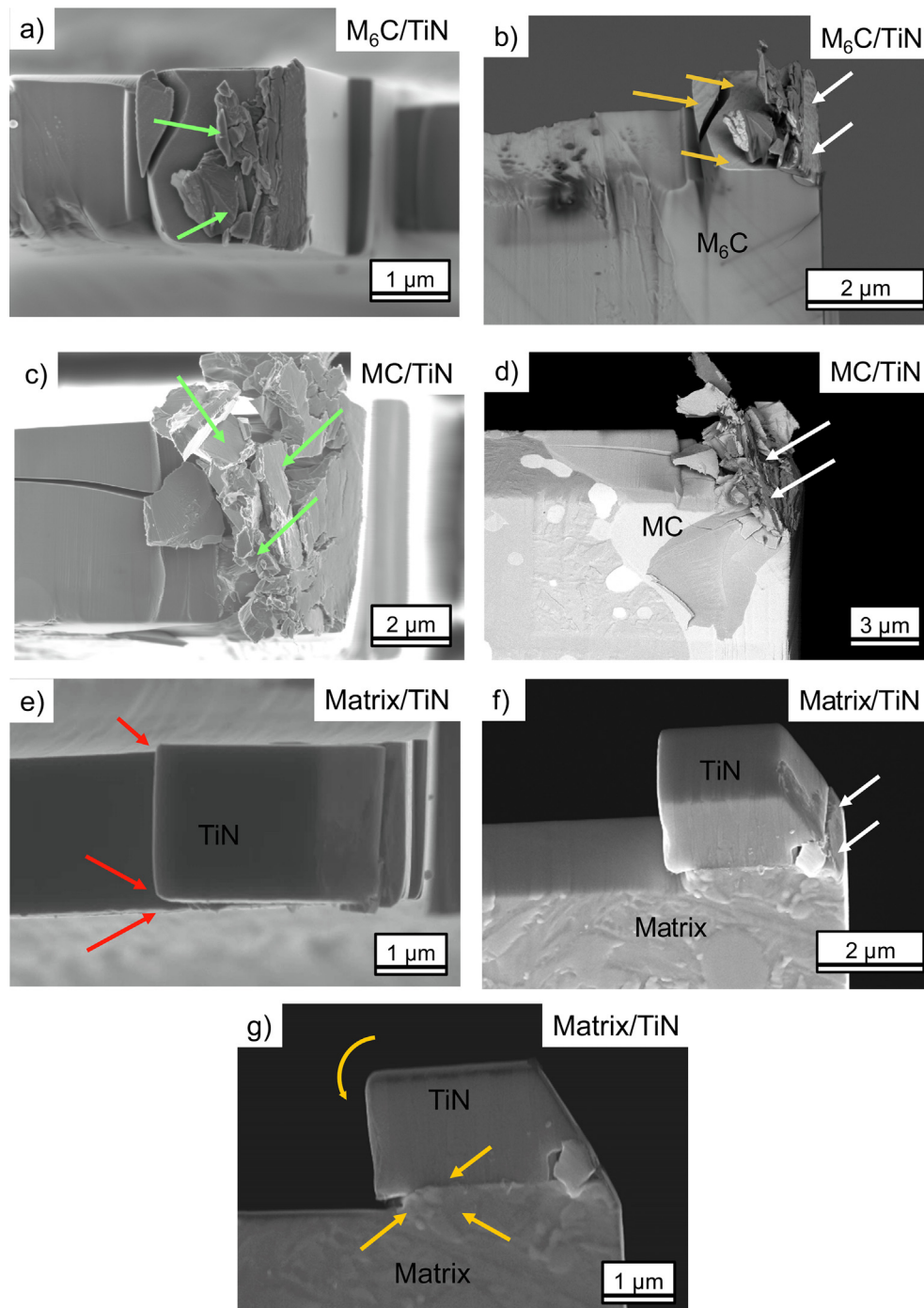
Fig. 7. SEM micrographs showing top and side views of a) the fractured M$_6$C/TiN MSC specimen with some remaining fragments of the TiN coating marked by green arrows; b) the fractured M$_6$C/TiN MSC specimen; c) the fractured MC/TiN MSC specimen with fragments of the MSC specimen marked by green arrows; d) the fractured MC/TiN MSC specimen; e) the deformed matrix/TiN MSC specimen with a intact but slightly rotated coating, see red arrows; f) the deformed matrix/TiN MSC specimen with a shift of the TiN coating in load direction; g) the deformed matrix/TiN MSC specimen with indications of a plastic deformation of the matrix, marked by orange arrows. The white arrows indicate the direction of loading and the region of plastic deformation that occurred in the specimen after the coating detachment due to the collision of specimen and flat punch indenter caused by the sudden release of the elastically stored energy at the moment of fracture (spring back, see Fig. 5). (For interpretation of the references to colour in this figure legend, the reader is referred to the web version of this article.)

and compression load. This choice is supported by the fact that tensile components are most relevant to crack opening and therefore failure in metals [43] and especially ceramic materials [44]. The obtained findings show a clear difference in failure and adhesion behaviour of the TiN coating on M$_6$C, MC carbides and the matrix of an HSS. Based on the experiments, it can be concluded that both the shear and compression loads that have to be applied to reach failure of the matrix/TiN interface are significantly lower compared

to those for the M$_6$C/TiN and for the MC/TiN MSC specimens, as evidenced by Table 3. Also note, that the stress values calculated using Eq. (1) are in good agreement with those determined in the FE simulations for zero residual stress within the coating. Fig. 7a) and b) infer that the fracture surface is equivalent to the interface of the M$_6$C/TiN MSC specimen. For the MC/TiN MSC specimen, the performed fractographic studies do not facilitate such a clear statement. Nevertheless, the calculated maximum principal
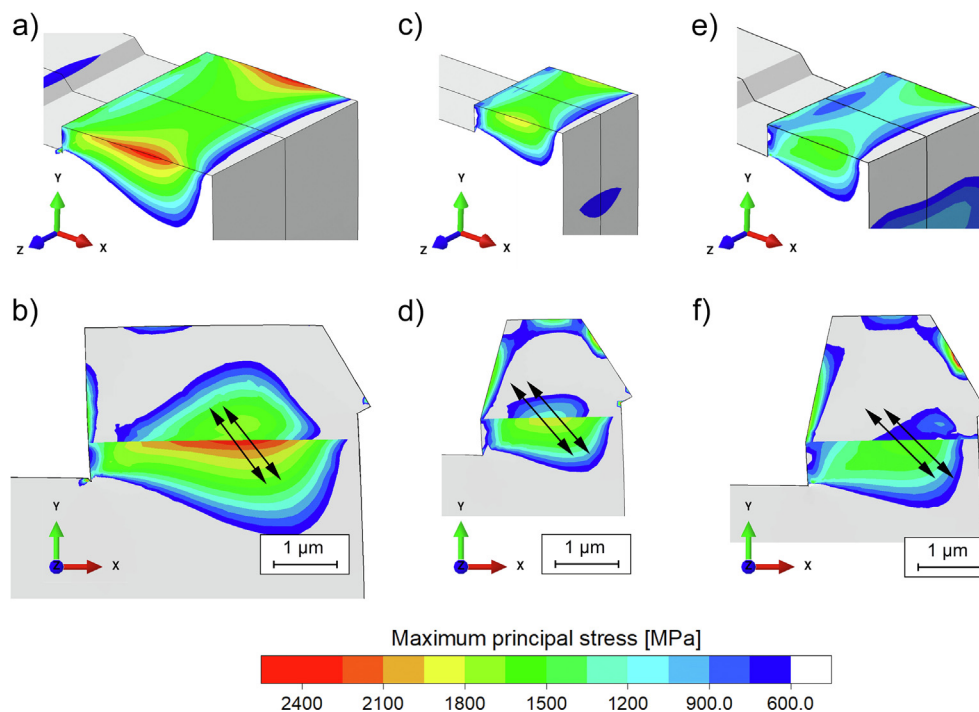
Fig. 8. Contour plots of the maximum principal stresses in the tested MSC specimens at the moment of maximum external load, a) and b) for the MC/TiN, c) and d) for the M_6C/TiN and e) and f) for the matrix/TiN MSC specimen. The directions of the maximum principal stress values that act in the interface are displayed by black arrows. For the interpretation of the colour grading we refer the reader to the online version of this article.
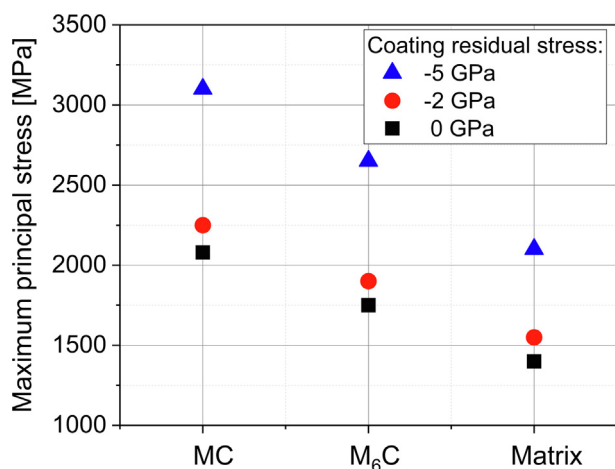

Fig. 9. Maximum principal stress values at the interface of indicated metal carbides and martensitic matrix towards a TiN hard coating as a function of the compressive residual stress in the coating.

stresses and the location of their most positive value at the interface, demonstrated in Fig. 8b), indicate that failure is likely to have originated from the substrate-coating interface in this case as well. Considering that especially in ceramic materials, unstable crack propagation occurs with considerable fractions of the speed of sound [46], it becomes clear that the origin of fracture cannot be directly determined from the SEM micrographs in Fig. 6. The observed failure behaviour, illustrated in Fig. 7, as well as the results of the FE simulations, shown in Fig. 8 and Fig. 9 indicate that the interface strength of the MC/TiN system is higher than that of the M_6C/TiN and that of the matrix/TiN system. This result confirms the findings of a beneficial effect of MC carbides on the adhesion of TiN coatings [18] due to an epitaxial growth of TiN on MC

carbide proposed in [19]. Epitaxially grown coatings represent high lattice coherence to the underlying substrate (e.g. $a_{TiN} \sim 4.24$ Å [19] and $a_{MC} \sim 4.17$ Å [47]) resulting in higher bond strength than incoherently grown coatings [48]. In contrast, the M_6C carbide has a cubic giant cell with a larger lattice parameter than TiN ($a_{M6C} \sim 11$ Å) [18,47,49,50], and thus has an incoherency with TiN [18,49,51] resulting in a lower bond strength compared to the MC/TiN system. Although shear and compressive stresses have been introduced into the MSC specimens, also tensile stresses occur at the interface between the TiN coating and the carbide, see Fig. 8 and Fig. 9. This can be explained by the occurrence of a constrained transversal strain in a direction perpendicular to the loading direction and a small bending contribution. Since the materials involved in the M_6C/TiN and MC/TiN interfaces are of ceramic nature and therefore are very sensitive to tensile stress [44], the calculated tensile stress components are likely to be mainly responsible for the coating's separation from the carbides. In the case of the matrix/TiN MSC specimen, plastification of the martensitic matrix occurred, as evident from Fig. 7e) to g) and the load–displacement curve shown in Fig. 5c). Furthermore, this plastification contributes to a reduction of the maximum principal stress acting at fracture of the interface between TiN and martensite. This leads to the lowest stress value for this interface in a ranking of the individual investigated microstructural constituents, as can be seen in Fig. 9. Nevertheless, dislocation pile-ups at the matrix-coating interface, resulting from plastification [52], can be assumed to lead to local tensile stresses, which support crack opening at the interface leading to coating decohesion [52].

Fig. 6e) and Fig. 6f) show mainly fracture fragments, as the pillar was destroyed by the collision of specimen and indenter after the fracture event. The amount of elastically stored energy scales with the pillars' dimensions, the carbides' and coatings' Young's modulus and the value of the applied load. The factors that lead to the observed stronger elastic spring back of the broken MSC specimen towards the flat punch indenter for the case of the MC/TiN pillar

can be explained by (i) its larger dimension compared to the M_6C/TiN MSC specimen [53], (ii) the higher Young's modulus of MC compared to M_6C [39] and (iii) the higher stresses at fracture for the MC/TiN MSC specimen. All these factors favour the more complete destruction of the MC/TiN MSC specimen compared to the M_6C/TiN and the matrix/TiN MSC specimen, respectively.

As described in section 2.1.2, the MSC specimen sizes differ between M_6C/TiN, MC/TiN and matrix/TiN. This was due to the intention to sample large, i.e. representative interface areas and therefore interface strength values to avoid the possible influence of the well-known size effect on strength [44]. Still, the maximum possible size of the produced MSC specimens was limited by the size of the individual microstructural constituents of the investigated HSS material. Note, that an influence of interfacial flaws on the observed fracture stresses cannot be excluded. For ceramics, the largest flaw leads to failure of the material [45]. For such brittle materials it is well-known that with smaller effectively loaded volumes or surfaces areas [54], fewer large defects affect the material's strength. Therefore, the observed strength values are higher compared to specimens with a large volume or surface area [53]. It is therefore necessary to refer to a representative volume or area, as otherwise the strength values may be misinterpreted. This representative volume is called "effective volume" or, as in the current study, in case of an area, the "effective area" [54]. At the interface of coated materials, there may be contaminations which can occur due to an insufficient cleaning process prior to the coating deposition and diminish the adhesion between substrate and coating [16]. Also, the inhomogeneities observed on the M_6C carbide that are associated with the grinding process could have a similar effect. Therefore, it is possible that strength values could be influenced by the effectively loaded interface area if different MSC specimen sizes are tested. However, a systematic study of this possible influence on the observed strength values was beyond the scope of the current work. Even though the exact dependence of the interface strength on the effectively tested area is currently unknown, the determined strength ranking is still reliable, since the investigated MC/TiN interface, that showed the highest strength value, also had the highest tested interface area, see Table 2. The other two used interface areas were smaller and about equal in size, which does not compromise the determined strength ranking, since the MC/TiN specimen with the largest interface area did exhibit the largest strength value.

All in all, it should be pointed out that the method presented within this study enables to determine local interface strength and interface failure of a substrate-coating system. Furthermore, an interface strength ranking between a hard coating and the microstructural constituents of e.g. a HSS was established. Considering possible future uses of the proposed technique, one may think of the following: In HSS materials the interface area between the martensitic matrix and the coating has a significant share of the total interface area between substrate and coating. This fact suggests the need to study a possible influence of the phase distribution in and the texture of the substrate's grains with respect to the coating plane. It should be mentioned, that also the influence of the surface condition resulting from preparation of the substrate prior to coating deposition, is a possible factor to be studied regarding its impact on the interfacial cohesion and calls for further work using the here proposed testing technique. For a more detailed understanding of the influence of the associated defect structures and orientation relationships on the interface strength behaviour, transmission electron microscopy studies of the structures resulting at the interface would be greatly beneficial. Finally, we want to point out that our approach involves considerable efforts, but in turn provides the possibility of a quantitative assessment of the strength values of planar interfaces in addition to a qualitative strength ranking that may be also obtainable by alternative to be developed methods, e.g. based on scratching techniques.

5. Conclusions

The current work presents a new test method to investigate the interface strength and interface failure of single components of a multi-component system under loads acting on real-world metalworking tools such as used for drilling or milling. Micromechanical tests, using a novel micro shear compression (MSC) specimen geometry, were conducted to determine the interface strength between a TiN coating and individual microstructural constituents of a high speed steel (HSS), i.e. M_6C and MC carbides as well as martensitic matrix. For the illustration of the stresses prevailing within the MSC specimen at fracture and to establish a strength ranking, FE simulation was carried out. Under combined shear- and compressive stress, tensile stresses are induced at the interface between substrate and coating, which lead to coating detachment that are therefore defined as interface strength. This enables to determine the failure stresses of specific interfaces for various substrate-coating systems. Based on the results obtained, a strength ranking of the interfaces between the microstructural constituents of HSS and a TiN hard coating was established:

$$MC/TiN > M_6C/TiN > martensite/TiN$$

The high strength of the MC/TiN interface is presumably caused by the high bonding strength associated with the epitaxy between TiN and MC, leading to higher adhesion of TiN on MC compared to M_6C and martensite.

CRediT authorship contribution statement

Matthias Gsellmann: Conceptualization, Methodology, Investigation, Validation, Visualization, Writing - original draft, Project administration. **Thomas Klünsner:** Conceptualization, Project administration, Supervision, Methodology, Writing - review & editing, Supervision, Funding acquisition. **Christian Mitterer:** Conceptualization, Writing - review & editing, Supervision. **Martin Krobath:** Methodology, Investigation, Visualization, Writing - review & editing. **Michael Wurmshuber:** Methodology, Investigation. **Harald Leitner:** Funding acquisition. **Werner Ecker:** Visualization, Writing - review & editing. **Stefan Marsoner:** Project administration, Funding acquisition, Writing - review & editing. **Verena Maier-Kiener:** Investigation, Visualization, Writing - review & editing. **Daniel Kiener:** Methodology, Investigation, Writing - review & editing. **Gerald Ressel:** Conceptualization, Project administration, Supervision, Writing - review & editing, Funding acquisition.

Declaration of Competing Interest

The authors declared that there is no conflict of interest.

Appendix A. Supplementary data

Supplementary data to this article can be found online at https://doi.org/10.1016/j.matdes.2021.109690.

References

[1] F. Klocke, Manufacturing Processes 1 - Cutting, RWTH, Springer-Verlag, Berlin Heidelberg, Aachen (2011), https://doi.org/10.1007/978-3-642-11979-8.

[2] K. Holmberg, A. Matthews, Coatings Tribology: Properties, Mechanisms, Techniques and Applications in Surface Engineering, 2nd ed.,., Elsevier, Amsterdam, 2009.

[3] D.A. Stephenson, J.S. Agapiou, Metal Cutting Theory and Practice, 3rd ed.,., CRC Press Taylor & Francis Group, Boca Raton, 2016.

[4] K. Bobzin, High-performance coatings for cutting tools, CIRP J. Manuf. Sci. Technol. 18 (2017) 1–9, https://doi.org/10.1016/j.cirpj.2016.11.004.

[5] A.W. Nemetz, W. Daves, T. Klünsner, W. Ecker, J. Schäfer, C. Czettl, T. Antretter, Cyclic heat-up and damage-relevant substrate plastification of single- and bilayer coated milling inserts evaluated numerically, Surf. Coatings Technol. 360 (2019) 39–49, https://doi.org/10.1016/j.surfcoat.2019.01.008.

[6] I. Krajinović, W. Daves, M. Tkadletz, T. Teppernegg, T. Klünsner, N. Schalk, C. Mitterer, C. Tritremmel, W. Ecker, C. Czettl, Finite element study of the influence of hard coatings on hard metal tool loading during milling, Surf. Coatings Technol. 304 (2016) 134–141, https://doi.org/10.1016/j.surfcoat.2016.06.041.

[7] T. Klünsner, M. Krobath, W. Ecker, S. Marsoner, M. Morstein, B. Marklein, Influence of localized cyclic substrate plastification on residual stress, load stress and cracking near the interface between hard coating and WC-Co hard metal substrate, Int. J. Refract Metal Hard Mater. 82 (2019) 113–120, https://doi.org/10.1016/j.ijrmhm.2019.04.003.

[8] S.J. Bull, E.G. Berasetegui, An overview of the potential of quantitative coating adhesion measurement by scratch testing, Tribol. Int. 39 (2006) 99–114, https://doi.org/10.1016/j.triboint.2005.04.013.

[9] A. Kleinbichler, M.J. Pfeifenberger, J. Zechner, S. Wöhlert, M.J. Cordill, Scratch induced thin film buckling for quantitative adhesion measurements, Mater. Des. 155 (2018) 203–211, https://doi.org/10.1016/j.matdes.2018.05.062.

[10] H. Javed, B. Merle, E. Preiß, R. Hivet, A. Benedetto, M. Göken, Mechanical characterization of metallic thin films by bulge and scratch testing, Surf. Coat. Technol. 289 (2016) 69–74, https://doi.org/10.1016/j.surfcoat.2016.01.051.

[11] H. Ollendorf, D. Schneider, A comparative study of adhesion test methods for hard coatings, Surf. Coat. Technol. 113 (1999) 86–102, https://doi.org/10.1016/S0257-8972(98)00827-5.

[12] Z. Chen, K. Zhou, X. Lu, Y.C. Lam, A review on the mechanical methods for evaluating coating adhesion, Acta Mech. 225 (2014) 431–452, https://doi.org/10.1007/s00707-013-0979-y.

[13] N. Vidakis, A. Antoniadis, N. Bilalis, The VDI 3198 indentation test evaluation of a reliable qualitative control for layered compounds, J. Mater. Process. Technol. 143–144 (2003) 481–485, https://doi.org/10.1016/S0924-0136(03)00300-5.

[14] R.F. Bunshah, Handbook of Hard Coatings: Deposition Technologies, Properties and Applications, Noyes Publications / William Andrew Publishing, LLC, New York (2001), https://doi.org/10.1016/S0301-679X(01)00021-4.

[15] M. Gsellmann, T. Klünsner, C. Mitterer, S. Marsoner, G. Skordaris, K. Bouzakis, H. Leitner, G. Ressel, Near-interface cracking in a TiN coated high speed steel due to combined shear and compression under cyclic impact loading, Surf. Coatings Technol. 394 (2020), https://doi.org/10.1016/j.surfcoat.2020.125854.

[16] C.W. Moura e Silva, E. Alves, A.R. Ramos, C.S. Sandu, A. Cavaleiro, Adhesion failures on hard coatings induced by interface anomalies, Vacuum 83 (2009) 1213–1217, https://doi.org/10.1016/j.vacuum.2009.03.010.

[17] R. Mesquita, Tool Steels: Properties and Performance, CRC Press Taylor & Francis Group, Boca Raton (2017), https://doi.org/10.1201/9781315181516.

[18] U. Helmersson, B.O. Johansson, J.-E. Sundgren, H.T.G. Hentzell, P. Billgren, Adhesion of titanium nitride coatings on high-speed steels, J. Vac. Sci. Technol., A 3 (1985) 308–315, https://doi.org/10.1116/1.573256.

[19] L. Hultman, H.T.G. Hentzell, J.-E. Sundgren, B.-O. Johansson, U. Helmersson, Initial growth of TiN on different phases of high speed steels, Thin Solid Films 124 (1985) 163–170, https://doi.org/10.1016/0040-6090(85)90259-7.

[20] D. Chicot, P. Démarécaux, J. Lesage, Apparent interface toughness of substrate and coating couples from indentation tests, Thin Solid Films 283 (1996) 151–157, https://doi.org/10.1016/0040-6090(96)08763-9.

[21] J. Schaufler, C. Schmid, K. Durst, M. Göken, Determination of the interfacial strength and fracture toughness of a-C: H coatings by in-situ microcantilever bending, Thin Solid Films 522 (2012) 480–484, https://doi.org/10.1016/j.tsf.2012.08.031.

[22] K. Matoy, T. Detzel, M. Müller, C. Motz, G. Dehm, Interface fracture properties of thin films studied by using the micro-cantilever deflection technique, Surf. Coatings Technol. 204 (2009) 878–881, https://doi.org/10.1016/j.surfcoat.2009.09.013.

[23] M.C. Liu, J.C. Huang, Y.T. Fong, S.P. Ju, X.H. Du, H.J. Pei, T.G. Nieh, Assessing the interfacial strength of an amorphous-crystalline interface, Acta Mater. 61 (2013) 3304–3313, https://doi.org/10.1016/j.actamat.2013.02.019.

[24] R. Konetschnik, R. Daniel, R. Brunner, D. Kiener, Selective interface toughness measurements of layered thin films, AIP Adv. 7 (2017), https://doi.org/10.1063/1.4978337.

[25] I. El Azhari, J. García, M. Zamanzade, F. Soldera, C. Pauly, C. Motz, L. Llanes, F. Mücklich, Micromechanical investigations of CVD coated WC-Co cemented carbide by micropillar compression, Mater. Des. 186 (2020), https://doi.org/10.1016/j.matdes.2019.108283.

[26] L.S. Qiu, X.D. Zhu, S. Lu, G.Y. He, K.W. Xu, Quantitative evaluation of bonding strength for hard coatings by interfacial fatigue strength under cyclic indentation, Surf. Coatings Technol. 315 (2017) 303–313, https://doi.org/10.1016/j.surfcoat.2017.02.045.

[27] H. Ur Rehman, F. Ahmed, C. Schmid, J. Schaufler, K. Durst, Study on the deformation mechanics of hard brittle coatings on ductile substrates using in-situ tensile testing and cohesive zone FEM modeling, Surf. Coatings Technol. 207 (2012) 163–169, https://doi.org/10.1016/j.surfcoat.2012.06.049.

[28] X. Zhang, B. Zhang, Y. Mu, S. Shao, C.D. Wick, B.R. Ramachandran, W.J. Meng, Mechanical failure of metal/ceramic interfacial regions under shear loading, Acta Mater. 138 (2017) 224–236, https://doi.org/10.1016/j.actamat.2017.07.053.

[29] M.B. Lazar, P. Xirouchakis, Mechanical load distribution along the main cutting edges in drilling, J. Mater. Process. Technol. 213 (2013) 245–260, https://doi.org/10.1016/j.jmatprotec.2012.09.020.

[30] S. Klima, N. Jäger, H. Hruby, C. Mitterer, J.F. Keckes, M. Burghammer, R. Daniel, Structure-stress relationships in nanocrystalline multilayered Al 0.7 Cr 0.3 N/Al 0.9 Cr 0.1 N coatings studied by cross-sectional X-ray nanodiffraction, Mater. Des. 170 (2019), https://doi.org/10.1016/j.matdes.2019.107702.

[31] S. Wurster, R. Treml, R. Fritz, M.W. Kapp, E. Langs, M. Alfreider, C. Ruhs, P.J. Imrich, G. Felber, D. Kiener, Novel Methods for the Site Specific Preparation of Micromechanical Structures, Pract. Metallogr. 52 (2015) 131–146, https://doi.org/10.3139/147.110331.

[32] B. Luo, Y. Li, K. Zhang, H. Cheng, S. Liu, A novel prediction model for thrust force and torque in drilling interface region of CFRP / Ti stacks, Int. J. Adv. Manuf. Technol. 81 (2015) 1497–1508, https://doi.org/10.1007/s00170-015-7294-9.

[33] K.D. Bouzakis, N. Vidakis, Prediction of the fatigue behaviour of physically vapour deposited coatings in the ball-on-rod rolling contact fatigue test, using an elastic-plastic finite elements method simulation, Wear 206 (1997) 197–203, https://doi.org/10.1016/S0043-1648(96)07494-7.

[34] J. Kabel, Y. Yang, M. Balooch, C. Howard, T. Koyanagi, K.A. Terrani, Y. Katoh, P. Hosemann, Micro-mechanical evaluation of SiC-SiC composite interphase properties and debond mechanisms, Compos. Part B Eng. 131 (2017) 173–183, https://doi.org/10.1016/j.compositesb.2017.07.035.

[35] W.C. Oliver, G.M. Pharr, An improved technique for determining hardness and elastic modulus using load and displacement sensing indentation experiments, J. Mater. Res. 7 (1992) 1564–1583, https://doi.org/10.1557/JMR.1992.1564.

[36] A. Leitner, V. Maier-Kiener, D. Kiener, Essential refinements of spherical nanoindentation protocols for the reliable determination of mechanical flow curves, Mater. Des. 146 (2018) 69–80, https://doi.org/10.1016/j.matdes.2018.03.003.

[37] Abaqus 2018, Dassault Syst. Simulia Corp. 2018. (n.d.). https://www.3ds.com/ (accessed October 7, 2020).

[38] K. Holmberg, A. Laukkanen, H. Ronkainen, K. Wallin, S. Varjus, J. Koskinen, Tribological contact analysis of a rigid ball sliding on a hard coated surface. Part II: Material deformations influence of coating thickness and young's modulus, Surf. Coatings Technol. 200 (2006) 3810–3823, https://doi.org/10.1016/j.surfcoat.2005.03.041.

[39] D. Casellas, J. Caro, S. Molas, J.M. Prado, I. Valls, Fracture toughness of carbides in tool steels evaluated by nanoindentation, Acta Mater. 55 (2007) 4277–4286, https://doi.org/10.1016/j.actamat.2007.03.028.

[40] H. Zhang, B.E. Schuster, Q. Wei, K.T. Ramesh, The design of accurate micro-compression experiments, Scr. Mater. 54 (2006) 181–186, https://doi.org/10.1016/j.scriptamat.2005.06.043.

[41] S.J. Bull, Failure mode maps in the thin film scratch adhesion test, Tribol. Int. 30 (1997) 491–498, https://doi.org/10.1016/S0301-679X(97)00012-1.

[42] J. Gerth, M. Larsson, U. Wiklund, F. Riddar, S. Hogmark, On the wear of PVD-coated HSS hobs in dry gear cutting, Wear 266 (2009) 444–452, https://doi.org/10.1016/j.wear.2008.04.014.

[43] R. Pippan, A. Hohenwarter, Fatigue crack closure: a review of the physical phenomena, Fatigue Fract. Eng. Mater. Struct. 40 (2017) 471–495, https://doi.org/10.1111/ffe.12578.

[44] R. Danzer, T. Lube, P. Supancic, R. Damani, Fracture of ceramics, Adv. Eng. Mater. 10 (2008) 275–298, https://doi.org/10.1002/adem.200700347.

[45] M.A. Meyers, K.K. Chawla, Mechanical Behavior of Materials, Cambridge University Press, Cambridge, 2009.

[46] B. Lawn, Fracture of brittle solids, 2nd ed., Cambridge University Press, Cambridge, 1993.

[47] M.M. Serna, J.L. Rossi, MC complex carbide in AISI M2 high-speed steel, Mater. Lett. 63 (2009) 691–693, https://doi.org/10.1016/j.matlet.2008.11.035.

[48] C. Schönjahn, L.A. Donohue, D.B. Lewis, W.-D. Münz, R.D. Twesten, I. Petrov, Enhanced adhesion through local epitaxy of transition-metal nitride coatings on ferritic steel promoted by metal ion etching in a combined cathodic arc/ unbalanced magnetron deposition system, J. Vac. Sci. Technol. A Vacuum, Surfaces, Film. 18 (2000) 1718–1723, https://doi.org/10.1116/1.582414.

[49] M.R. Ghomashchi, C.M. Sellars, Microstructural changes in as-cast M2 grade high speed steel during high temperature treatment, Met. Sci. 18 (1984) 44–48, https://doi.org/10.1179/030634584790420339.

[50] D.H. Jack, K.H. Jack, Invited review: Carbides and nitrides in steel, Mater. Sci. Eng. 11 (1973) 1–27, https://doi.org/10.1016/0025-5416(73)90055-4.

[51] P.H. Mayrhofer, F. Kunc, J. Musil, C. Mitterer, A comparative study on reactive and non-reactive unbalanced magnetron sputter deposition of TiN coatings, Thin Solid Films 415 (2002) 151–159, https://doi.org/10.1016/S0040-6090(02)00511-4.

[52] A. Misra, J.P. Hirth, R.G. Hoagland, Length-scale-dependent deformation mechanisms in incoherent metallic multilayered composites, Acta Mater. 53 (2005) 4817–4824, https://doi.org/10.1016/j.actamat.2005.06.025.

[53] G. Dehm, B.N. Jaya, R. Raghavan, C. Kirchlechner, Overview on micro- and nanomechanical testing: New insights in interface plasticity and fracture at small length scales, Acta Mater. 142 (2018) 248–282, https://doi.org/10.1016/j.actamat.2017.06.019.

[54] G.D. Quinn, Weibull effective volumes and surfaces for cylindrical rods loaded in flexure, J. Am. Ceram. Soc. 86 (2003) 475–479, https://doi.org/10.1111/j.1151-2916.2003.tb03324.x.